Nanoscale

Plasmonic Enhancement of Nitric Oxide Generation

Journal:	*Nanoscale*
Manuscript ID	NR-ART-04-2021-002126.R1
Article Type:	Paper
Date Submitted by the Author:	11-Jun-2021
Complete List of Authors:	Knoblauch, Rachael; University of Maryland Baltimore County Department of Chemistry and Biochemistry, ; University of Maryland Baltimore County Institute of Fluorescence, Department of Chemistry and Biochemistry Geddes, Chris; University of Maryland Baltimore County, Institute of Fluorescence

Plasmonic Enhancement of Nitric Oxide Generation

*Rachael Knoblauch and Chris D. Geddes**

Institute of Fluorescence and Department of Chemistry and Biochemistry, University of Maryland Baltimore County, 701 East Pratt Street, Baltimore, Maryland 21202, USA

*all correspondence: geddes@umbc.edu

KEYWORDS: nitric oxide, carbon nanodots, reactive nitrogen species, photosensitization, metal-enhanced fluorescence, plasmon, silver nanoparticles.

ABBREVIATIONS:

NO•	–	Nitric Oxide
ME-NO•	–	Metal-enhanced Nitric Oxide (release)
RNS	–	Reactive Nitrogen Species
ROS	–	Reactive Oxygen Species
BrCND	–	Brominated Carbon Nanodots (brominated dots)
RNS	–	Reactive
DAF-FM	–	Diaminofluorescein-FM
DAF-T	–	Triazole product of reacted DAF-FM probe

Abstract

While the utility of reactive oxygen species in photodynamic therapies for both cancer treatments and antimicrobial applications has received much attention, the inherent potential of reactive nitrogen species (RNS) including nitric oxide (NO•) for these applications should not be overlooked. In recent years, NO• donor species with numerous—including photodynamic—mechanisms have been classified with efficacy in antimicrobial and therapeutic applications. While properties of NO• delivery may be tuned structurally, herein we describe for the first time a method by which photodynamic NO• release is amplified simply by utilizing a plasmonic metal substrate. This is a process we term "metal-enhanced nitric oxide release," or ME-NO•. Using donor agents known as brominated carbon nanodots (BrCND), also the first carbon nanodot variation classified to release NO• photodynamically, and the *fluorescence-on* probe DAF-FM, we report metal-enhanced release of NO• 2- to 6-fold higher than what is achieved under classical conditions. Factors affecting the plasmon-amplified photodynamic system are subsequently studied, including exposure times, excitation powers, and surface area, and consistent ME-NO• factors are reported from BrCND across these tunable conditions. Only probe concentration is determined to impact the detected ME-NO• factor, with higher concentrations resulting in improved detectability of "actual" NO• release enhancement. Further, principles of metal-enhanced fluorescence (MEF) are applied to achieve a faster, high-throughput experimental method with improved data resolution in ME-NO• detection. The results have significant implications for the improvement of not just carbon nanodot NO• donor agents, but a wide spectrum of photoactivated NO• donor systems as well.

38 **1.0 Introduction**

39 Photodynamic therapies, and antimicrobial photodynamic therapies, are increasingly well-
40 characterized and efficacious options in the treatment of cancers[1-3] and microbial infections.[4-6] These
41 methods typically rely on the generation of reactive oxygen species (ROS), such as singlet oxygen,
42 superoxide anion radical, and hydroxyl radical to name a few.[7] The therapeutic applications of reactive
43 nitrogen species (RNS) such as nitric oxide (NO•) are in recent years receiving attention; the release of
44 NO•, for example, finds utility in the treatment of atherosclerosis and ischemia related diseases, both
45 improved via the modulation of endogenous NO• availability;[8, 9] downstream products of NO• also are
46 helpful in cancer therapies for enhancing DNA, mitochondrial, and cell apoptosis and necrosis.[10, 11]
47 Beyond therapeutics, NO•-donating molecules have found relevance in antimicrobial applications as
48 well.[12-16] Characterized by broad-spectrum antimicrobial activity, NO• donors have a similar potential as,
49 and even a synergistic potential with ROS to combat the growing trend of antibiotic resistance in bacterial
50 infections. In fact, much antibacterial character of RNS is associated with the products generated via the
51 reaction of NO• with ROS.[15] A number of NO•-donating structures exist, including photo-responsive
52 compounds,[8, 17] pH-dependent structures,[17] and others such as metal-organic frameworks.[18] Given both
53 that ROS generation is often photodynamically triggered and the advantages inherent to a multi-
54 mechanism antimicrobial agent in achieving potency, focus should be placed on the creation and
55 characterization of photodynamically activated NO• donor species—particularly those that may also
56 generate ROS.

57 Carbon nanodot structures present a promising scaffold for the development of such a compound.
58 These quasi-spherical nanoparticles composed of oxidized graphene sheets are collected as combustion
59 byproducts[19, 20] or products of biomass processing;[21] inexpensive to collect, they are frequently presented
60 as a "green" option for various applications.[22-24] While typically tuned for luminescence properties,

61 applications have extended recently to ROS photosensitization for antimicrobial materials.[25-27] In a recent
62 report from our laboratory, brominated carbon nanodot (BrCND) structures were found to generate ROS
63 from both type I (electron transfer) and type II (energy transfer) photosensitization processes, exhibiting
64 light-activated toxicity both against Gram-positive *Staphylococcus aureus* and *Listeria monocytogenes*,
65 as well as Gram-negative *Escherichia coli.* Intriguingly, BrCND were also reported for the first time to
66 release NO•. Although this occurred primarily via a pH-dependent mechanism, slightly higher NO•
67 detection was reported when the pH cycle was combined with an irradiation procedure.[28] The BrCND
68 therefore present an intriguing new structure for the tandem release of *both* ROS and RNS, for the broad-
69 spectrum antimicrobial activity. To bolster the efficacy of these particles as antimicrobials, we have
70 recently investigated plasmon amplification as a strategy for higher ROS yields, reporting the metal-
71 enhanced generation of singlet oxygen from BrCND.[29] This method follows similar principles as metal-
72 enhanced fluorescence (MEF), where proximity of fluorophores to surface plasmons in the near-field
73 permits fluorophore-nanoparticle coupling, resulting in enhanced emission and absorption (local field
74 enhancement) mechanisms and higher fluorescence emission intensities.[30] This strategy has been
75 employed previously with such ROS photosensitizers as identified in *ESI Appendix* Table S1, for both
76 type I and type II photosensitization products, but has regrettably not yet been investigated *hitherto* for
77 photodynamic NO• donors.

78 Herein, we probe the photodynamic release of NO• (both under classical and plasmon-amplified
79 regimes) from BrCND using the *fluorescence-on* probe 4-amino-5-methylamino-2′,7′-difluorofluorescein
80 (DAF-FM). In the presence of dissolved oxygen, generated NO• induces the formation of a triazole
81 derivative of DAF-FM (simply, DAF-T) essentially irreversibly, substantially improving the quantum
82 yield and subsequently the probe fluorescence intensity upon excitation.[31] Using this method, relative
83 quantities of NO• release may be monitored over set irradiation intervals for different experimental

84 conditions. This permits characterization of NO• generation from a carbon nanodot structure, as we will
85 describe, and reveals more generally the *hitherto* unreported ability of plasmonic substrates to amplify the
86 photodynamic release of NO•. Further, we employ principles of MEF to achieve more rapid NO•, and
87 indeed ME-NO•, detection. This is the first report of an inter-plasmon-donor interaction as a strategy of
88 amplifying NO• generation. The significance of our approach is further realized by the fact that inter-
89 plasmon amplification can potentially be applied to virtually any existing photodynamic NO• donor
90 system.

91 **2.0 Materials and Methods**

92 **Sample and Solvent Preparation.** Brominated carbon nanodots (BrCND) were collected and pH-
93 adjusted as reported previously;[28] briefly, a Bunsen burner connected to a laboratory gas outlet was placed
94 under a collection funnel with a vacuum applied such that the gaseous biproducts of combustion were
95 bubbled through a collection solvent (Hydrobromic acid). This collection was conducted for 6-hours, and
96 the resulting solution adjusted to pH 3.0 using a trisodium citrate buffer solution and aliquots of 10M HBr
97 and NaOH as needed (final concentrations: $[Na_3Cit] = 0.16$ M $[Br-]_{max} = 0.4_5$ M). The solution pH was
98 monitored using an Accumet® Basic AB15 benchtop pH meter. 4-Amino-5-Methylamino-2',7'-
99 Difluorofluorescein (DAF-FM) was purchased from Invitrogen and the stock concentration prepared
100 according to manufacturer recommendations; subsequent dilution into anhydrous dimethyl sulfoxide
101 resulted in a stock concentration of 500 μM.

102 **Metal-Enhanced Nitric Oxide Release: Classical Detection, Single Sample.** To perform the
103 detection experiments with pH cycling, a buffered solution of BrCND was first adjusted to pH 12-12.5
104 using small (<5% total volume) aliquot of 10M NaOH. An aliquot of 500 μM DAF-FM was then added
105 to achieve a ~7 μM final concentration, and 50 μL aliquots were added to the wells of either a blank 96-
106 well plate ("dark" samples) or an exposure plate (either a blank or Quanta Plate™ (silvered substrate)

107 depending on the trial). For pH cycled samples, a small aliquot of 10M HCl was added to both dark and
108 exposure well samples; an equivalent volume of deionized water was added to dilution cycle control
109 samples. The exposure plate was then placed under an Entela Blak-Ray® Long Wave Ultraviolet lamp
110 (Model B 100 AP/R, λ_{ex} = 365 nm) for a 4 minute exposure period (prior to beginning the experiment,
111 exposure wells were selected to standardize exposure powers using a ThorLabs PM100D power meter).
112 During exposure, samples were maintained at ~20°C using an ice bath heat sink. It should be noted that
113 at the concentrations used, for both brominated carbon nanodots and DAF-FM, the absorption intensities
114 (at 365 nm) and approximate pathlength of the ~50 μL samples (~2.5 mm) are not sufficient to produce
115 inner filtering effects; as such, it is likely that the 365 nm excitation source used for these experiments is
116 able to activate metal nanoparticle plasmons. Immediately after exposure, pH cycle samples were adjusted
117 back to basic pH using 10M NaOH (with an equal volume of deionized water added to dilution cycle
118 samples). All samples were then diluted 5x with deionized water, transferred individually to a quartz
119 cuvette, and fluorescence spectra recorded using a FluoroMax®-4P spectrophotometer (λ_{ex} = 475 nm, 2
120 nm slit widths). Throughout the experiment, solution pH was monitored using pH paper; laboratory lights
121 were switched off and the stock probe maintained under desiccated conditions to prevent probe
122 degradation. This same procedure was conducted for all other ME-NO• experiments with the following
123 modifications:

124 All results reported in this study (with the exception of *ESI Appendix,* Fig. S2) were performed
125 without pH cycling. As such, no additional aliquots of NaOH or HCl were added to any sample after the
126 initial pH adjustment to 12-12.5 described previously.

127 Exposure times, exposure powers, and exposure surface areas are varied for different data sets
128 reported herein. In all cases, the relevant value for each variable is specified. In the case of exposure times,
129 all samples were added to the exposure well simultaneously, and covered completely by black electrical

130 tape at various intervals. For exposure power, this variable was tuned by selecting exposure wells located
131 in various positions under the UV lamp, and power recorded using the power meter mentioned previously.
132 Surface area was tuned by creating masks from black electrical tape and adhering these masks to the
133 surface of the relevant well. For all masks, percent area exposure (100% = full well opening) was
134 calculated by a smaller inner circle set within the area of the full well opening; templates were printed on
135 adhesive paper and cut from electrical tape by hand using a utility knife (see Fig3*C* for mask schematic).
136 Surface area. (*SA)*, time (*t*), and power (*P*) were all used to calculate energy density (*ED*) for each
137 condition, as reported. For experiments involving concentration adjustment of DAF-FM, only the initial
138 aliquot volume of DAF-FM was changed. In all cases, reported values are the average of all individual
139 trials, with error from standard deviation.

140 **Metal-Enhanced Nitric Oxide Release: High-Throughput.** Experiments were all conducted as
141 described previously, with the following modification for the final detection step:

142 After exposure, all samples were prepared for detection as described previously. In lieu of transfer
143 to a quartz cuvette, 80 μL of each sample was transferred to a new well of both a blank and Quanta Plate™.
144 Similar to what was discussed previously, the pathlength of the 80 μL samples (~4 mm) and absorption
145 intensities of each agent in solution were not sufficient to attenuate the excitation wavelengths employed
146 for DAF-FM excitation described here; accordingly, the Quanta Plates™ could also be used for metal-
147 enhanced *detection* of NO• release. Using a Varian Cary Eclipse Florescence spectrophotometer equipped
148 with a plate reader, first the blank then the Quanta Plate™ were analyzed spectrally using the following
149 parameters: λ_{ex} = 280 nm, λ_{em} = 480-550 nm, automatic excitation/emission filters, PMT voltage = 800
150 V, slit widths = 5 nm, scan rate = 0.1 sec, CAT mode = 5 scans). This strategy is indicated in the text as
151 "high-throughput, spectral" analysis. For this method, reported values are also the average (and standard
152 deviation) of all trials. Alternatively, samples were more rapidly analyzed using the "advanced read"

153 feature within the Varian Cary Eclipse Florescence software; parameters for this analysis are as follows:
154 λ_{ex} = 280 nm, λ_{em} = 513 nm, automatic excitation/emission filters, PMT voltage = 800 V, slit widths = 5
155 nm, scan rate = 1 sec. Readings for each trial were reported as the average of 5 scans per sample, with
156 error from standard deviation. In this case, all trial values were averaged, and error propagated through all
157 analysis and calculations (see next section) to final values.

158 To select the parameters for HT detection, synchronous scattering ($\lambda_{ex} = \lambda_{em}$) spectra from the
159 silvered wells (containing 80 μL of buffer control solution) and the absorption spectrum of DAF-FM were
160 also collected. For the former, the Varian Cary Eclipse Florescence spectrophotometer was used with the
161 following parameters: λ_{range} = 200-800 nm, automatic filters, excitation and emission slit widths = 1.5 nm
162 and 2.5 nm respectively. Absorption measurements were recorded for a basic DAF-FM/BrCND buffered
163 solution in a quartz cuvette using a Agilent Technologies Cary 60 UV-Vis spectrophotometer with Cary
164 WinUV Scan application software.

165 **Data Analysis and Calculations.** A minimum of N = 3 trials were performed for each
166 experimental condition and is specified for each data set. Independently, the spectra (both "dark" and
167 "exposed") for each trial were normalized to the "dark" condition spectrum ("dark" or ED = 0 J•cm^{-2}, max
168 = 1). The normalized spectra for replicate trials were then averaged, with error bars reported from standard
169 deviation. Percent signal changes (ΔS, %) for each condition were calculated according to Eq. **1**

$$\Delta S, \% = \left(I_{ED\neq 0,i} - I_{ED=0,i}\right)/I_{ED=0,i} * 100 \qquad \textbf{[1]}$$

170 where I indicates raw fluorescent intensity recorded at 513 nm and i indicates the exposure conditions of
171 either a blank 96-well plate ($i = blank$) or a Quanta Plate™ ($i = Ag$). These values are reported as averages
172 of a minimum of N = 3 trials, with error from standard deviation. ME-NO• factors ($F_{NO\bullet}$) were also
173 calculated independently according to Eq. **2**

$$F_{NO\bullet} = \Delta S_{Ag}/\Delta S_{Blank} \quad [2]$$

with reported values the average of all trial calculations for each measured condition.

Characterization of Metal-Enhanced Fluorescence and DAF-FM. To ensure that the DAF-T structure was dominant in solution for detection and characterization of metal-enhanced *fluorescence* (MEF) of the probe in Quanta Plates™, a DAF-FM/BrCND solution was prepared as described previously, using a DAF-FM concentration of 10 μM. At basic pH, 80 μL aliquots were added to both blank and silvered wells for fluorescence detection using the high-throughput spectral method (λ_{ex} = 280 nm). The samples were then pH adjusted to <3.0 and equilibrated at this pH for ~1 min to produce DAF-T; this was followed by an adjustment back to basic pH and final high-throughput spectral detection. MEF factors (F_j) for both structures were calculated for each trial individually according to Eq. **3**

$$F_j = I_{j,Ag}/I_{j,Blank} \quad [3]$$

where fluorescence intensity (I) was recorded at 513 nm, and j indicates either DAF-FM or DAF-T. A total of N = 5 trial MEF factors were averaged and reported, with error from standard deviation.

Statistical Analysis. For determination of P values, a two tailed, paired t-test was performed for each data set. P values are rounded conservatively to regular confidence intervals.

3.0 Results

Metal-Enhanced Release of Nitric Oxide. In order to preliminarily assess the ability of BrCND to release nitric oxide photodynamically, the DAF-FM *fluorescence-on* probe was added to a concentrated solution of BrCND. The sample underwent a pH cycle in order to optimize detection of the probe (at basic pH), and to permit release of nitric oxide (at acidic pH), e.g., an "exposed" sample would begin at basic pH, undergo an acid addition to lower pH to <3.0, then be placed under a 365 nm UV lamp for exposure. Following this interval, pH would then be returned to basic. As a control, a dilution cycle was also

194 performed where an aliquot of deionized water was added rather than acid, i.e., the sample remains at
195 basic pH for the duration of the experiment. This procedure was conducted previously, albeit at a more
196 dilute concentration of BrCND, in our earlier report;[28] in this system, we noted that the UV-exposed
197 sample generated a stronger probe response under pH-cycled conditions, indicating a small but significant
198 photodynamic mechanism of NO• release (*ESI Appendix,* Fig. S1). At this concentration of BrCND,
199 however, there was no significant photodynamic release mechanism observable under dilution-cycle
200 parameters. Conversely, at a higher concentration of BrCND (~10-fold greater), there is no significant
201 difference in probe intensity under *pH-cycled* conditions; the dilution-cycle parameters instead reveal a
202 strong and significant increase in fluorescence intensity for the exposed versus dark control sample (*ESI*
203 *Appendix*, Fig. S2). The comparability of the pH-cycled samples is likely simply due to kinetics; at higher
204 concentrations of BrCND, the pH-dominated NO• release mechanism results in probe saturation
205 (approaching complete conversion to the reacted form, DAF-T), where a secondary, weaker photodynamic
206 mechanism is not observable through experimental error. When the pH-dependent release of NO• is not
207 occurring, the photodynamic mechanism is more clearly observed. The detection of NO• from brominated
208 carbon nanodots under each set of conditions does indeed highlight both release mechanisms for these
209 structures; this is intriguing although not unexpected. NO• donor molecules are known to operate via both
210 pH-triggered and light-activated pathways,[17, 32, 33] as we see for the carbon dots here. A more detailed
211 discussion of possible NO• release mechanisms is presented in our earlier publication.[28]

212 The investigation of metal-enhanced NO• release described herein was then conducted using *only*
213 dilution-cycle parameters from this point onward. UV exposure was conducted (365 nm, 240 sec, 530 ±
214 10 μW) either in a blank 96-well plate or a Quanta Plate™, which features a silvered substrate surface on
215 the well bottoms that are optimized (commercially) for metal-enhanced fluorescence (MEF). Recently, as
216 previously mentioned, these Quanta Plates™ were applied by our laboratory in the detection of metal-

enhanced singlet oxygen (ME-$^1O_2$) also from brominated carbon nanodots at this UV-A wavelength.[29] It is interesting to note that typically silver plasmonic materials are employed in MEF applications for visible wavelength coupling and amplification; this is due to the localized surface plasmon resonance (LSPR) properties of silver nanoparticles, which peak in the range of 400-500 nm. Although not optimized for UV applications, our previous report demonstrated that the Quanta Plates™ were able to scatter 365 nm light. Further, the potential for brominated dots to generate singlet oxygen diminishes with increasingly long-wavelength (approaching 400 nm) exposure sources; this is due to decreased absorption intensities of the nanodots, and is illustrated through the detection of phosphorescence from the nanodots in an O_2 diffusion-limited environment.[34, 35] In the context of singlet oxygen enhancement, we were able to achieve plasmonic amplification from the silvered Quanta Plates™ in conjunction with brominated carbon nanodots and 365 nm light, suitably tuning the experimental parameters for compatibility between each component.[29] The application of Quanta Plates™ then to enhancement of NO• generation was a reasonable extension. ME-NO• release from BrCND was thus detected using this method; the normalized intensities of post-exposure DAF-FM/DAF-T solutions are shown in Fig. 1*B*. For both exposure conditions, the resulting spectrum increases notably; however, a significantly higher intensity is achieved by the Quanta Plate™ samples—that is, the metal-enhanced samples. When calculating the percent signal change (relative to that detected under dark conditions), 200 ± 40% and 100 ± 20% increases were observed for Quanta Plate™ and blank plate samples respectively (Fig. 1*C*). Corresponding to these data is a 2-fold increase in NO• release in the plasmon-amplified regime ($P < 0.04$), or a ME-NO• factor equal to 2.

We were then curious how varying the parameters of exposure would affect the detected ME-NO• factor within a system. We began by varying the exposure time, conducting fluorescence measurements for DAF-FM/DAF-T solutions at 40 second intervals up to the 240 second maximum (Fig. 2). Although the percent signal changes increased roughly logarithmically for both blank- and Quanta Plate™

exposures as time increased (Fig. 2*A*), the ME-NO• factor did not vary in tandem. Rather, a ME-NO• factor of 2.0 ± 0.1 was reported as the average for measured time points; no significant difference was found for the factors calculated at any individual time point (Fig. 2*B*).

Exposure parameters for photosensitization experiments are frequently reported in terms of energy density (J•m^{-2}), which is calculated simply according to Eq **4**

$$ED = (P \times t)/SA \qquad \textbf{[4]}$$

where *P, t,* and *SA* are exposure power, time, and sample surface area respectively. MEF, and indeed ME-ROS generation, are known to follow the excitation volumetric effect [36]; thus, it seemed plausible that varying either power or surface area may produce results different from those detected by varying time alone. To probe this, three values of energy density were chosen and tested using the previously described set up (parameters can be found in *ESI Appendix* Table S2). For each system, two of the variables (*P/t/SA*) were held constant while the third was tuned to achieve the desired energy density. The results in terms of signal change are reported in Fig. 3*A-C*. Intuitively, both varied time (0-240 sec, 80 sec intervals) and power (~580, 950, 1600 μW) follow trends previously described to the time variable, increasing in percent signal change as energy density is increased. When surface area is varied, however, the inverse trend is observed for both blank- and Quanta Plate™ conditions. This is expected as energy density is inversely proportional to surface area; therefore, the total exposure volume decreases for higher energy density samples, *however*, the entire solution volume is still available for diffusion of the reacted probe DAF-T. ME-NO• factors were also calculated for these conditions, as reported in Fig. 3*D*. The condition for each independent experiment where all parameters were equal is bolded in this panel (1200 J•m^{-2}). Surprisingly, all ME-NO• factors in this condition were not equal between experiments; this points to a degree of expected experimental variation due to a number of factors, including variability of "true" probe

concentration, which is not known (manufacturer guidelines indicate a concentration of ~5mM upon first rehydration) and may be impacted by probe instability in aqueous solvents. Nonetheless, these reported values average to a ME-NO• factor of 2.0 ± 0.8, equivalent to that discussed earlier in this report. ME-NO• factors for both 2200 and 3300 J•m^{-2} values as well are not significantly different, and it can be considered that under these varied conditions the detected metal-enhancement of NO• release is independent of these parameters. Only the variation of surface area resulted in any non-zero linear trendline (*ESI Appendix* Table S2) and would merit closer investigation as a subject of a future report.

Due to the irregularity found experimentally in the 1200 J•m^{-2} condition, we were then curious if probe concentration could impact the overall detection of ME-NO• release (Fig. 3*E*). Using the parameters for 1200 J•m^{-2}, we performed identical experiments varying only the initial concentration of DAF-FM. Concentrations ranging from 1-10 μM produced ME-NO• factors near to what was detected previously, ranging from 1.5 ± 0.1 to 1.9 ± 0.3 for 1 and 10 μM samples respectively. This range confirms what was postulated earlier: that probe concentration variation may be responsible for the range of detected ME-NO• values. Interestingly, further increasing the DAF-FM concentration also increases the detected ME-NO• factor to as high as 6 ± 1 for the 100 μM sample. This likely does not reflect any variation in the "true" plasmonic enhancement of NO• release alone, but rather the kinetics of the detection system. BrCND, as nanoparticles, have a much lower diffusion rate than small molecules in general; fluorescein, for example, has a diffusion coefficient of ~4•10^{-6} cm^{2}•sec^{-1} in water.[37, 38] NO•, by comparison, diffuses even faster, with reported rates of ~2•10^{-5} cm^{2}•sec^{-1} in PBS and water.[39] With diffusion of NO• rather than the probe dictating its reactivity with DAF-FM, higher probe concentrations are required to detect NO• molecules before they encounter another species with which to react. Simply, with a higher concentration of DAF-FM, it becomes more probable that NO• will react with a probe molecule within the experimental window, permitting more accurate detectability of the enhanced NO• released on Quanta Plates™ than is

284 possible at lower concentrations. Thus, while ME-NO• is detected and reported herein, the reported values
285 are likely conservative.

286 **Metal-Enhanced Detection of ME-NO• Release.** While not discussed to this point, the
287 aforementioned strategy for the detection of NO• release from BrCND required a time-consumptive
288 procedure whereby each sample was analyzed individually; this required laborious cleaning steps between
289 samples and limited the throughput of each experiment. This "single sample" detection method (diagram
290 in *ESI Appendix* Fig. S3*A*) led to a total experimental time of ~2 hours (*ESI Appendix* Table S3) for a
291 procedure and data set such as that described by Fig. 3*A*. The adoption of a high-throughput, 96-well plate
292 method for detection is preferrable due to significantly reduced analysis time; for example, the same
293 experiment run using a spectrophotometer equipped with a plate reader improved analysis time (for all
294 samples) from ~1.6 hours to 25 ± 2 min in the case where full spectra were collected ("HT, spectral," *ESI*
295 *Appendix* Fig. S3*B* and Table S3). The expediency of this process could be further improved to 12.6 ± 0.8
296 min by adopting a "high-throughput, advanced read" method (*ESI Appendix* Fig. S3*C*), which collected
297 *only* the intensity of a sample at 513 nm.

298 The use of high-throughput methods using a *fluorescence-on* assay presents the chance to employ
299 the principles of MEF to improve detectability. To test this possibility using DAF-FM/DAF-T, we first
300 sought to optimize the parameters for use of a Quanta Plate™ rather than a blank plate in fluorescence
301 detection (*ESI Appendix* Fig. S4). An ideal excitation wavelength would be well-absorbed by the
302 fluorophore while also being minimally scattered by the substrate; although scattered excitation can be
303 helpful in achieving higher MEF values—i.e., the enhanced absorption effect—when using low
304 concentration or low-emitting fluorophores, scattered excitation can cause significant distortion in the
305 sample background. This was detected in our case, testing an initial excitation wavelength of 475 nm, as
306 used previously (*ESI Appendix* Fig. S4*B*, top); therefore, this excitation wavelength for DAF-FM/DAF-T

307 is not a viable parameter for the metal-enhanced *detection* of NO•. In contrast to metal-enhanced
308 generation of reactive species, however, MEF processes can occur not just by the amplification of incident
309 excitation light, but also through the enhanced emission mechanism. By this mechanism, fluorophore
310 quanta couples to the nanoparticle plasmon to radiate as a unit. In the MEF literature, this leads to modified
311 radiative decay rates and improved quantum yields.[40-42] In our case, employing silvered Quanta Plates™
312 is highly desirable in DAF-FM/DAF-T MEF applications, since probe emission occurs at visible
313 wavelengths. As mentioned previously, this corresponds well with typical LSPR properties of silver
314 nanoparticle substrates. To optimize for *emission*, rather than excitation, enhancement, an excitation
315 wavelength of 280 nm was tested. This wavelength is still absorbed by the probe, resulting in a detectable
316 fluorescence intensity at 513 nm in the excitation profile (*ESI Appendix* Fig. S4*A*). Excitation scattering
317 by the substrate, as identified by the synchronous scattering spectral profile ($\lambda_{ex} = \lambda_{em}$), also predicted
318 much lower background as a result of this wavelength. When DAF-FM emission was collected using this
319 wavelength, the background signal was negligible at 513 nm emission, and a clearly defined spectral
320 profile was detected (*ESI Appendix* Fig. S4*B*, bottom). All subsequent high-throughput experiments were
321 therefore conducted using this parameter.

322 It is common for fluorophores with varying structure to feature different MEF factors in proximity
323 to the same substrate. In the case of simple plasmon-enhanced detection (without any element of metal-
324 enhancement of analyte, as with ME-NO• release), this is not so problematic as the enhancement simply
325 improves detectability, and a system may be calibrated for quantitation. When a plasmon-amplified
326 photodynamic process is also occurring, it becomes difficult to distinguish if what is being detected is
327 metal-enhancement of the probe *fluorescence* only, enhancement of the photodynamic process, or—*more*
328 *likely*—a mixture of both. In the case of ME-NO• detection, this may be accounted for by using the proper
329 controls if the enhancement factor of both DAF-FM and DAF-T are known. Accordingly, we collected

330 the fluorescence spectra of DAF-FM on both blank- and Quanta Plates™, excited at 280 nm (Fig. 4*A*,
331 top); subsequently, the fluorescence of a DAF-FM sample from a pH-cycled BrCND solution (i.e., a
332 predominately DAF-T solution) was also collected in classical (blank) and MEF (Quanta Plate™) regimes
333 (Fig. 4*A*, bottom). Both sets of spectra displayed an increase for the sample detected in Quanta Plate™
334 wells as predicted. When MEF factors were calculated there was no significant difference between that
335 reported for DAF-FM (1.6 ± 0.5) and DAF-T (1.9. ± 0.1), although a 10-fold improvement in relative
336 standard deviation (RSD, 30 vs. 3% for DAF-FM vs. DAF-T respectively) was found (Fig. 4*B*). Since
337 fluorescence enhancement can be considered equal for both forms of the probe, calculations of percent
338 signal changes and ME-NO• factors are indeed simplified.

339 Having completed these MEF characterization steps for the DAF-FM based NO• detection system,
340 we then proceeded to conduct both high-throughput spectral and advanced read methods of detecting this
341 phenomenon from BrCND and silvered substrates. This was conducted using the variable time
342 experimental strategy, with energy densities of 0 (0 sec exposure), 1200 (80 sec), 2500 (160 sec), and
343 3600 (240 sec) J•m^{-2} (Fig. 5). As shown in Fig. 5*A* for classical exposure conditions (no ME-NO• release),
344 signal increases are observable proportional to longer exposure times for both blank- and Quanta Plate™
345 *detection*; stronger signals are, however, observed from the Quanta Plates™, confirming MEF from the
346 DAF-FM/DAF-T solutions, and improving signal to noise. Full data sets were collected using the
347 advanced read method detected in both classical (blank) and MEF (Quanta Plate™) detection regimes,
348 and the resulting calculated ME-NO• factors are reported in Fig. 5*B*. The results are consistent with the
349 single sample spectral method described earlier, with blank detection values of 2 ± 1, ± 1, and ± 0.9 for
350 1200, 2500, and 3600 J•m^{-2} respectively. Notably similar values were also determined for the MEF
351 detection system, with values of 1.6 ± 0.6, 1.5 ± 0.4, and 1.7 ± 0.4 for 1200, 2500, and 3600 J•m^{-2}
352 respectively. RSD improved from the 60 ± 10% inherent to blank detection by half to 29 ± 5% in silvered

Quanta Plate™ wells. In this case, as with the high-throughput spectral method illustrated in Fig. 5*A*, signal to noise is improved in the detection of ME-NO• release from BrCND using a MEF platform.

4.0 Discussion

Nitric oxide has a number of therapeutic and antimicrobial applications as outlined in the introduction. Regarding BrCND, release of this agent has illustrated a potential avenue for secondary antimicrobial activity in tandem with the release of reactive oxygen species.[28] Even if weakly bactericidal, NO• is a precursor for many downstream reactive species, some of which are shown by reaction schemes **1-4**:

$$2NO\bullet \rightarrow O_2 + 2NO_2 \quad \textbf{[1]}$$

$$2NO_2 + 2NO\bullet \rightleftharpoons 2N_2O_3 \quad \textbf{[2]}$$

$$2N_2O_3 + 2H_2O \rightarrow 4NO_2^- + 4H^+ \quad \textbf{[3]}$$

$$O_2^{\bullet -} + NO\bullet \rightarrow ONOO^- \quad \textbf{[4]}$$

The study described here was undertaken specifically to understand the potential tunability of the antimicrobial response from various reactive species, emphasizing the photodynamic behavior of NO• release from BrCND. While the pH-dependent response has been previously characterized, we sought to probe the photodynamic mechanism, first by better identifying its presence in a basic, high-BrCND concentration study, where the pH-dependency is not at play (Fig. S2). That both pH- and photodynamic release of NO• are detected from BrCND hints to their structural complexity; NO• donors are classified to proceed via both of these mechanisms, depending on their structure.[17] Despite this photodynamic mechanism of NO• generation, to date, no attention has been given in the literature to tuning NO• release from donors via metal-enhancement, also known as plasmon amplification, an inter-plasmon-donor mechanism. This stands in contrast to ME-ROS generation,[36] which has been explored for a multitude of

371 photosensitizers and reactive species (*ESI Appendix,* Table S1). The detection of ME-NO• release from
372 BrCND marks the first report of ME-NO• from a donor species to the best of the authors' knowledge,
373 having first characterized this phenomenon herein using a 4 minute UV-exposure interval in both blank-
374 and Quanta Plate™ wells (Fig. 1). Using the DAF-FM *fluorescence-on* probe, enhancement is observed
375 via the significantly stronger percent signal change of the UV-exposed plasmonic system versus its blank
376 plate counterpart (Fig. 1*C*).

377 Further investigation on the impact of exposure time in a ME-NO• system confirmed that the
378 detected ME-NO• factor is not dependent upon exposure time (Fig. 2). This is significant, as predictable
379 quantities of enhanced NO• release could be possible for well-defined donor molecules with minimal
380 variability, simply accounting for overall changing donor concentrations and NO• quantum yields. As
381 photo-activatable donor molecules are designed and implemented in various future ME-NO• hybrid
382 systems, however, this feature will require characterization due to possible degradation of the
383 enhancement properties, i.e., consistency of the plasmonic material over time. Exposure properties of
384 power and surface area were also probed to assess their potential impact on the overall detected NO•
385 release enhancement effect (Fig. 3*B-D*). Given the excitation-dependent nature of photodynamic
386 processes, one might expect that these two variables would have a considerable impact on detected
387 enhancement of NO• release. It is well-known that the enhanced absorption effect is one mechanism by
388 which plasmonic amplification of luminescence (and other processes) occurs [42-44]. This mechanism would
389 indeed be impacted by both exposure powers and surface area. Remarkably, under the studied conditions
390 variation of neither of these results in a ME-NO• factor substantially distinct (Fig. 3*D*), and in fact
391 concentration of the probe itself seems to be a larger determining parameter in the resulting detected factor
392 (Fig. 3*E*). These results suggest, as proposed earlier, that the *detectability* of enhancement, rather than
393 "true" enhancement itself, is dictated predominantly by the concentrations of probe available to react with

394 the released NO•; thus, the true enhancement of NO• released could be, and is likely, much higher than
395 anticipated from these studies. This is not problematic for antimicrobial applications, as an under-
396 estimation nonetheless confirms the potential for metal-enhanced photoactivated antimicrobial activity
397 from amplified NO• release. The results are impactful not only in further bolstering the potential
398 application of BrCND as a photo-activatable antimicrobial material, but also in encouraging researchers
399 to explore the cultivation of new NO• (or other photodynamically released species) donor molecules for
400 use in plasmon-amplified systems.

401 The multiplicity of use for plasmonic platforms is also highlighted herein. Not only may the
402 substrate enhance overall release of NO•, but it also can be employed to circumvent experimental
403 limitations. We explored this possibility using the detection of NO• generation by *fluorescence-on* probe
404 DAF-FM by both single sample and high-throughput analysis methods. When comparing data gathered
405 by both methods (Fig. 1-3 versus Fig. 5) it is clear that the signal to noise ratio is superior for the single
406 sample detection method employed; however, the total analysis time is improved substantially. Whereas
407 a single sample (including sample transfer, detection, disposal, and cleaning) is performed in ~3 minutes,
408 a total of 16 samples may be run in 12 ± 1 minutes using a high throughput method of spectral detection
409 (*ESI Appendix* Table S3). This corresponds to ~45 seconds per sample, a 4-fold improvement in total
410 analysis time. It is important to note here the differences in data quality obtained by each of these methods.
411 In order to optimize collection time by the high throughput spectral method, a relatively rapid scan rate
412 was chosen to accommodate the averaging of 5 total scans per sample. While the scan averaging improves
413 signal to noise, the more rapid collection diminishes this feature. This is visible in the spectra collected in
414 blank 96-well plates (Fig. 5*A*, left). Use of a metal nanoparticulate substrate, employing a MEF system in
415 detection (Fig. 5*A*, right), improves the signal to noise ratio and therefore the data quality obtained by this
416 method. This can be attributed logically to the 2-fold fluorescence enhancement factors we report for both

417 DAF-FM and DAF-T (Fig. 4). Using MEF, the detection system itself helps to offset the time versus
418 resolution trade off. The improvement in analysis time and data quality may be further refined using the
419 high-throughput "advanced read" method, whereby only intensities at a select wavelength are read; using
420 a slower scan rate and still collecting 5 scans per sample, the total analysis time decreases to ~24 seconds
421 per scan (*ESI Appendix* Table S3). Using blank plate detection, even with this method, does not reduce
422 error such that calculated ME-NO• factors have acceptable deviation (Fig. 5*B*). When MEF detection is
423 employed, conversely, the relative standard deviation is improved significantly, resulting more clearly
424 resolved calculated values. Moreover, the ME-NO• factors determined by this method match those
425 collected in previous experiments using the single sample methodology, confirming the MEF detection
426 strategy as a valid and competitive option for similar detection applications.

427 **5.0 Conclusion**

428 Our results underscore the potential for widespread applications of metal-enhanced hybrid photo-
429 activatable agents through the use of an inter-plasmon-donor system. BrCND, previously characterized to
430 photodynamically generate ROS and to release NO• in a pH-dependent manner, are shown also to have a
431 secondary photodynamic mechanism of NO• release. While the use of carbon nanodot structures as RNS
432 donors has not *hitherto* been extensively explored, the impact of these results is further reinforced through
433 the detection of the plasmon-amplified release of NO• using the commercially available silvered Quanta
434 Plate™ wells. Similar plasmonic material-modified platforms have been used to probe metal-enhanced
435 ROS generation in the literature, although comparable systems for RNS have not been analogously
436 characterized. Employing this approach, we present considerations for classifying the overall
437 enhancement of photodynamic processes—in this case, ME-NO•—including excitation power, exposure
438 time, and surface area of exposure. Future studies may investigate these same principles for ME-NO•
439 using colloidal metal nanoparticles, or nanoparticle-donor molecule hybrid systems. Regarding the

440 reported system, concentration of the detection probe is also considered relative to calculated ME-NO•
441 and is in fact identified as the limiting feature in classifying ME-NO• release factors from brominated
442 carbon nanodots. Further, the experimental limitations such as analysis time and resolution are improved
443 for ME-NO• detection by employing a MEF-based high throughput detection system. The results
444 discussed herein not only describe the successful plasmonic amplification of NO• release, but further
445 describe a strategy for and key parameters of amplifying the activity of nearly any photodynamic donor
446 agent through our inter-plasmon-donor approach.

447

448 **ASSOCIATED CONTENT**

449

450 **Electronic Supplementary Information**

451 Supporting figures (S1-S4) are provided, demonstrating the photodynamic release of nitric oxide from
452 brominated carbon nanodots; a schematic for the different detection regimes is given, with additional
453 characterization and analysis for the metal-enhanced detection regime. Further, tables (S1-S3) are
454 provided to supply additional details into the literature reports of metal-enhanced photosensitization,
455 experimental parameters employed, and experimental times for studies discussed. ESI references are
456 included. Captions to all supplementary information are provided below:

457 **Figure S1.** Nitric oxide (NO•) detection from brominated carbon nanodots (BrCND) under pH cycled
458 conditions. Detection was completed using diaminofluorescein-FM (DAF-FM) probe both "pre" and "post"
459 acid cycling conditions, either under dark or UV-exposed (λ_{ex} = 365 nm, 0.56 ± 0.04 mW) conditions. *A)*
460 Fluorescence spectra of NO• detection under dark conditions. *B)* Average intensities from n = 3 trials, with
461 error from standard deviation (*p < 0.05). Reproduced from Ref. [S1] with permission from The Royal
462 Society of Chemistry.

463 **Figure S2.** Photodynamic release of nitric oxide (NO•) from brominated carbon nanodots (BrCND) as
464 detected by *fluorescence-on* probe DAF-FM. Release was detected after 4 minutes of either dark or UV
465 exposure ("Exposed," λ_{ex} = 365 nm, 580 ± $20_{(SD)}$ μW) in blank 96-well plates, both under dilution (pH ~
466 12-12.5) and pH cycled (pH < 3) conditions. $N = 5$, $*P << 0.001$, error from standard deviation.
467 **Figure S3.** Schematic of the different detection methods of metal-enhanced nitric oxide (ME-NO•)
468 photodynamic release from brominated carbon nanodots (BrCND), using the *fluorescence-on* probe DAF-
469 FM. Methods include *(A)* single sample, *(B)* high-throughput (HT) spectral detection, and *(C)* HT advanced
470 read, with detection occurring at 513 nm (error from standard deviation of $N = 5$ sample scans).
471 **Figure S4.** Selection of excitation parameters for metal-enhanced detection of nitric oxide (NO•) release.
472 *(A)* Spectral overlay of DAF-FM absorption (detected in blank plate, dashed blue line), excitation (detected
473 in Quanta Plate™, λ_{em} = 513 nm, solid blue line) profiles versus Quanta Plate™ well synchronous scattering
474 profile ($\lambda_{ex} = \lambda_{em}$). *(B)* Background excitation scattering versus DAF-FM (10 μM) emission in Quanta
475 Plate™ wells at λ_{ex} = *top* – 475 and *bottom* – 280 nm. Arrows indicate signal change relative to background
476 excitation scattering. All error from standard deviation from $N = 3$ measurements.
477 **Table S1.** Metal-Enhanced Generation or Release of Reactive Species.
478 **Table S2.** Parameters and Analysis from Varied Energy Density Experiments (Fig. 3).
479 **Table S3**. Timescales for Detection of Metal-Enhanced Nitric Oxide Release.
480

481 **Corresponding Author.**

482 *Tel: (410) 576-5723, Fax: (410) 576-5722, Email: geddes@umbc.edu

483

484 **Author Contributions.**

485 All experiments were designed by Rachael Knoblauch under the mentorship of Dr. Chris D. Geddes.
486 Experiments, data analysis and figure presentation were executed by Rachael Knoblauch. The manuscript

was written and edited by Rachael Knoblauch; additional review and editing was conducted by Dr. Chris D. Geddes.

Conflicts of Interest.

There are no conflicts of interest to declare.

Acknowledgments

This work was supported by the National Science Foundation Graduate Research Fellowship Program (2018262827) and the HHS/NIH/National Institute of General Medical Sciences (NIGMS) through the Chemistry/Biology Interface Program at the University of Maryland Baltimore County (5T32GM066706). The authors also acknowledge the Institute of Fluorescence (IoF) as well as the Department of Chemistry and Biochemistry at the University of Maryland Baltimore County (UMBC) as sources of internal funding.

References

1. K. Berg, P. K. Selbo, A. Weyergang, A. Dietze, L. Prasmickaite, A. Bonsted, B. Ø. Engesaeter, E. Angell-Petersen, T. Warloe, N. Frandsen and A. Høgset, *Journal of Microscopy*, 2005, **218**, 133-147.
2. P. Mróz and M. R. Hamblin, *Advances in Photodynamic Therapy: Basic, Translational, and Clinical*, Artech House, Inc, Boston, 2008.
3. R. Baskaran, J. Lee and S.-G. Yang, *Biomaterials Research*, 2018, **22**, 25-25.
4. Z.-J. Zhao, Z.-P. Xu, Y.-Y. Ma, J.-D. Ma and G. Hong, *PLoS ONE*, 2020, **15**, 1-19.
5. G. Cheng and B. Li, *Materials Today Advances*, 2020, **6**, 100049.
6. M. M. Awad, A. Tovmasyan, J. D. Craik, I. Batinic-Haberle and L. T. Benov, *Applied Microbiology And Biotechnology*, 2016, **100**, 7679-7688.
7. M. S. Baptista, J. Cadet, P. Di Mascio, A. A. Ghogare, A. Greer, M. R. Hamblin, C. Lorente, S. C. Nunez, M. S. Ribeiro, A. H. Thomas, M. Vignoni and T. M. Yoshimura, *Photochemistry & Photobiology*, 2017, **93**, 912-919.
8. A. Keszler, B. Lindemer, N. Hogg, D. Weihrauch and N. L. Lohr, *Archives of Biochemistry and Biophysics*, 2018, **649**, 47-52.
9. A. G. Herman and S. Moncada, *European Heart Journal*, 2005, **36**, 1945-1955.
10. E. B. Kang, G. B. Lee, I. In and S. Y. Park, *European Polymer Journal*, 2018, **101**, 96-104.

11. Y. Zhang, J. Yang, T. Meng, Y. Qin, T. Li, J. Fu and J. Yin, *European Journal of Medicinal Chemistry*, 2021, **212**, 113153.
12. V. F. Cardozo, C. A. Lancheros, A. M. Narciso, E. C. Valereto, R. K. Kobayashi, A. B. Seabra and G. Nakazato, *International Journal of Pharmaceutics*, 2014, **473**, 20-29.
13. M. T. Pelegrino, J. C. Pieretti, G. Nakazato, M. C. Gonçalves, J. C. Moreira and A. B. Seabra, *Nitric Oxide*, 2021, **106**, 24-34.
14. L. M. Estes, P. Singha, S. Singh, T. S. Sakthivel, M. Garren, R. Devine, E. J. Brisbois, S. Seal and H. Handa, *Journal of Colloid And Interface Science*, 2021, **586**, 163-177.
15. F. C. Fang, *The Journal of clinical investigation*, 1997, **99**, 2818-2825.
16. A. B. Seabra, M. T. Pelegrino and P. S. Haddad, in *Antibiotic Resistance: Mechanisms and New Antimicrobial Approaches*, eds. K. Kon and M. Rai, Academic Press, Elsevier Inc., Cambridge, MA, USA, 2016, ch. 9, pp. 187-204.
17. J. A. Hrabie and L. K. Keefer, *Chemical Reviews*, 2002, **102**, 1135-1154.
18. J. Chen, D. Sheng, T. Ying, H. Zhao, J. Zhang, Y. Li, H. Xu and S. Chen, *Nano-Micro Letters*, 2021, **13**, 1-17.
19. H. Zhang, J. Liang, J. Liu, S. Chen, H. Zhang, Z. Tian, Y. Cai, P. Wang, Y. Ye and C. Liang, *RSC Advances*, 2016, **6**, 8456-8460.
20. P. Roy, P.-C. Chen, A. P. Periasamy, Y.-N. Chen and H.-T. Chang, *Materials Today*, 2015, **18**, 447-458.
21. C.-C. Huang, Y.-S. Hung, Y.-M. Weng, W. Chen and Y.-S. Lai, *Trends in Food Science & Technology*, 2019, **86**, 144-152.
22. P. Devi, A. Thakur, S. K. Bhardwaj, S. Saini, P. Rajput and P. Kumar, *Journal of Materials Science-Materials in Electronics*, 2018, **29**, 17254-17261.
23. S. Lee, *Journal of Industrial and Engineering Chemistry*, 2019, **77**, 365-370.
24. X. Wen, L. Shi, G. Wen, Y. Li, C. Dong, J. Yang and S. Shuang, *Sensors & Actuators: B. Chemical*, 2015, **221**, 769-776.
25. J. Zhang, X. Lu, D. Tang, S. Wu, X. Hou, J. Liu and P. Wu, *ACS Applied Materials and Interfaces*, 2018, **10**, 40808-40814.
26. M. M. Al Awak, P. Wang, S. Wang, Y. Tang, Y.-P. Sun and L. Yang, *RSC Advances*, 2017, **7**, 30177-30184.
27. D. I. Abu Rabe, M. M. Al Awak, F. Yang, P. A. Okonjo, X. Dong, L. R. Teisl, P. Wang, Y. Tang, N. Pan, Y.-P. Sun and L. Yang, *International Journal of Nanomedicine*, 2019, **14**, 2655-2665.
28. R. Knoblauch, A. Harvey, E. Ra, K. M. Greenberg, J. Lau, E. Hawkins and C. D. Geddes, *Nanoscale*, 2021, **13**, 85-99.
29. R. Knoblauch, A. Harvey and C. D. Geddes, *Plasmonics*, 2021.
30. Y. Jeong, Y.-M. Kook, K. Lee and W.-G. Koh, *Biosensors and Bioelectronics*, 2018, **111**, 102-116.
31. S. M. Namin, S. Nofallah, M. S. Joshi, K. Kavallieratos and N. M. Tsoukias, *Nitric Oxide*, 2013, **28**, 39-46.
32. P. Ceccherelli, M. Curini, M. C. Marcotullio, F. Epifano and O. Rosati, *Synthetic Communications*, 1998, **28**, 3057-3064.
33. C. Parisi, M. Seggio, A. Fraix and S. Sortino, *ChemPhotoChem*, 2020, **4**, 742-748.
34. R. Knoblauch, E. Ra and C. D. Geddes, *Physical Chemistry Chemical Physics*, 2019, **21**, 1254-1259.
35. R. Knoblauch, B. Bui, A. Raza and C. D. Geddes, *Physical Chemistry Chemical Physics*, 2018, **20**, 15518-15527.
36. C. D. Geddes and J. Karolin, *Physical Chemistry Chemical Physics*, 2013, **15**, 15740-15745.
37. T. Casalini, M. Salvalaglio, G. Perale, M. Masi and C. Cavallotti, *Journal of Physical Chemistry B*, 2011, **115**, 12896-12904.
38. S. A. Rani, B. Pitts and P. S. Stewart, *Antimicrobial Agents and Chemotherapy*, 2005, **49**, 728-732.
39. G. Z. Ian and M. D. William, *Annals of Biomedical Engineering*, 2005, **33**, 214-222.
40. A. Dragan and C. D. Geddes, *Applied Physics Letters*, 2012, **100**, 093115.

564 41. E. C. Le Ru, P. G. Etchegoin, J. Grand, N. Félidj, J. Aubard and G. Lévi, *Journal of Physical Chemistry C*,
565 2007, **111**, 16076-16079.
566 42. E. C. Le Ru, J. Grand, N. Félidj, J. Aubard, G. Lévi, A. Hohenau, J. R. Krenn, E. Blackie and P. G. Etchegoin,
567 in *Metal-Enhanced Fluorescence*, ed. C. D. Geddes, John Wiley & Sons, Inc., Hoboken, NJ, USA, 2010, ch.
568 2, pp. 25-65.
569 43. Y. Zhao, A. Wang, J. Kang, H. Chu, H. Zhang and Y. Zhao, *Journal of Photochemistry & Photobiology, A:*
570 *Chemistry*, 2020, **400**, 112678.
571 44. M. Weisenberg, Y. Zhang and C. D. Geddes, *Applied Physics Letters*, 2010, **97**, 133103.

572

573

FIGURES AND TABLES

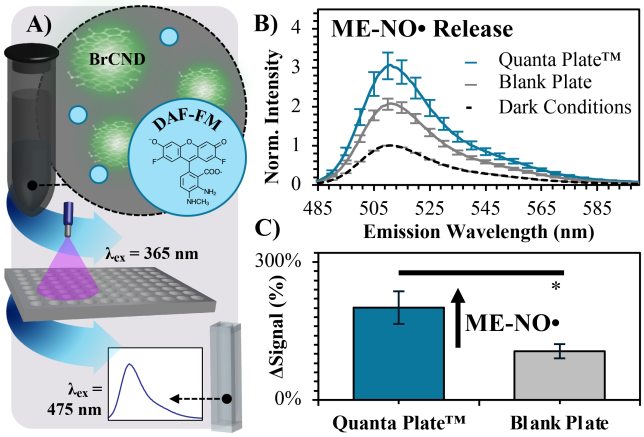

Figure 1. Metal-enhanced nitric oxide (ME-NO•) release from brominated carbon nanodots (BrCND). *(A)* Experimental schematic of single-sample NO• generation and detection methods. *(B)* Photodynamic (λ_{ex} = 365 nm, 530 ± 10 (SD) μW, 240 sec) release of NO• by BrCND in classical (blank) and plasmon-enhanced (quanta) exposure conditions, as reported by fluorescence-on spectral response of NO• probe DAF-FM (concentration of generation = 7 μM, λ_{ex} = 475 nm). *(C)* Percent signal change (relative to dark conditions) for each exposure regime ($\lambda_{ex/em}$ = 475/513 nm). N = 3, error from SD, *P < 0.04.

587

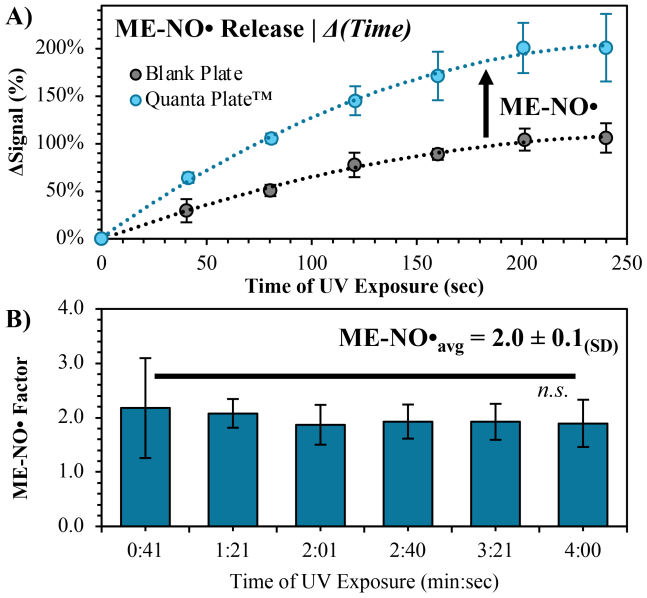

588
589

590 **Figure 2.** Time-dependent metal-enhanced nitric oxide (ME-NO•) release from brominated carbon nanodots
591 (BrCND), detected by DAF-FM (generation concentration = 7 μM, λ_{ex} = 475 nm). *(A)* Percent signal change
592 ($\lambda_{ex/em}$ = 475/513 nm) resulting from UV exposure (λ_{ex} = 365 nm, 560 ± 20 (SD) μW) for both classical
593 (blank) and plasmon-amplified (quanta) regimes; at each time point, $P < 0.04$; $N = 3$, error from SD. *(B)*
594 Corresponding ME-NO• factors for each time point from (A); $N = 3$, error from standard deviation.

595

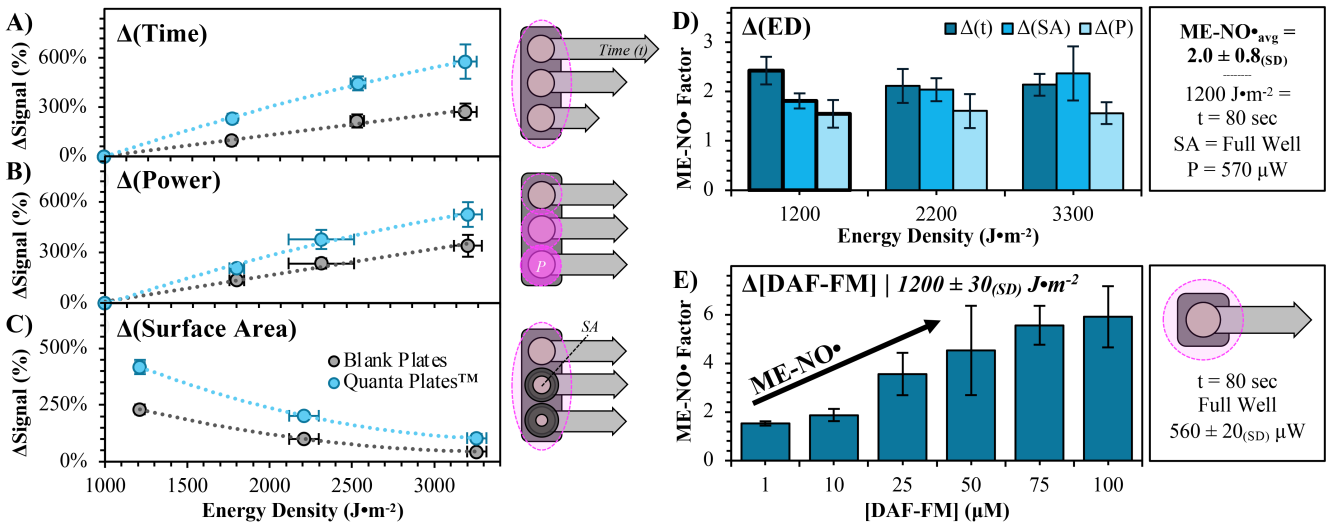

Figure 3. Metal-enhanced nitric oxide (ME-NO•) generation from brominated carbon nanodots: dependence of enhancement on exposure parameters. *(A-C)* Percent signal change of DAF-FM (7 µM) with UV (λ_{ex} = 365 nm) exposure in both blank and Quanta Plate™ wells, plotted as a function of energy density (ED); schematics provided on right, $N = 4$, error from standard deviation. ED was varied by tuning parameters of exposure *(A)* time (t), *(B)* power (P), and *(C)* surface area (SA). *(D) Left* - Calculated ME-NO• factor for systems reported in (A-C); *right* – averaged ME-NO• factor for all systems and parameters for ED at which all experiments have equal parameters (bolded data in *left*). *(E) Left* - ME-NO• factors calculated for systems of varying DAF-FM concentrations; *right* – experimental schematic and parameters for *left* data, at 1200 ± 30 (SD) J•m^{-2}.

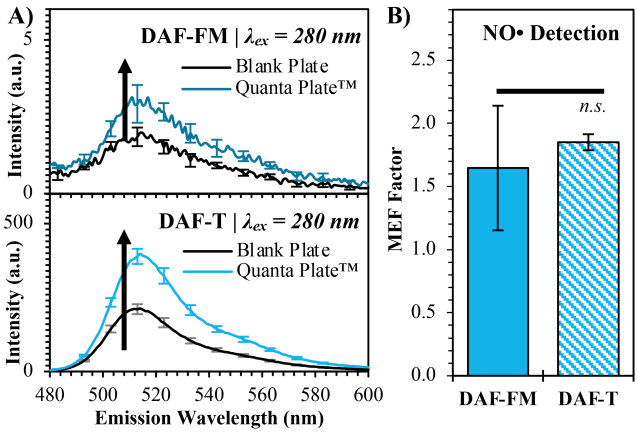

Figure 4. Enhancement factor comparison of un-reacted DAF-FM *fluorescence-on* probe versus the nitric oxide (NO•) reacted probe derivative (DAF-T), detected in Quanta Plate™ wells. *(A)* Sample spectra for metal-enhanced fluorescence (MEF) for *top* – DAF-FM and *bottom* - DAF-T. *(B)* MEF factors calculated for each probe structure (P = 0.5, not significant, n.s.) For all panels: error from standard deviation of N = 5 trials.

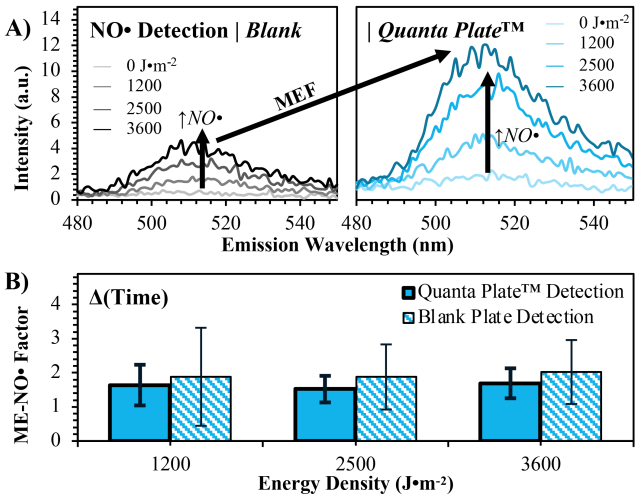

Figure 5. Application of metal-enhanced fluorescence (MEF) in the detection of nitric oxide (NO•) release from brominated carbon nanodots using fluorescence-on probe DAF-FM. *(A)* Sample high-throughput emission spectra from DAF-FM reacted with NO• under classical photodynamic release conditions at varying exposure times (reported as energy density); spectra are from $N = 5$ averaged scans for a single trial. *Left* – classical (blank plate) detection of NO• release; *right* – metal-enhanced detection of NO• release. *(B)* Improvement of calculated metal-enhanced NO• (ME-NO•) release factors from data collected by high-throughput classical (blank plate, RSD = $60 \pm 10_{(SD)}$%) or MEF (Quanta Plate™ RSD = $29 \pm 5_{(SD)}$%) detection regimes.